

# Simple Treatments of the Photon Noise and the Pixelation Effect in Weak Lensing

Jun Zhang<sup>\*</sup>

*Department of Astronomy, University of California, Berkeley, CA 94720, USA*

13 September 2022

## ABSTRACT

We propose easy ways of correcting for the systematic errors caused by the photon noise and the pixelation effect in cosmic shear measurements. Our treatment of noise can reliably remove the noise contamination to the cosmic shear even when the flux density of the noise is comparable with those of the sources. For pixelated images, we find that one can accurately reconstruct their corresponding continuous images by interpolating the logarithms of the pixel readouts with either the Bicubic or the Bicubic Spline method. The cosmic shears measured from the interpolated continuous images contain negligible systematic errors as long as the pixel size is about less than the scale size of the point spread function (PSF, including the pixel response function), a condition which is almost always satisfied in practice. Our methodology is well defined regardless of the morphologies of the galaxies and the PSF. Despite that our discussion is based on the shear measurement method of Zhang (2008), our way of treating the noise can in principle be considered in other methods, and the interpolation method that we introduce for reconstructing continuous images from pixelated ones is generally useful for digital image processing of all purposes.

**Key words:** cosmology: gravitational lensing - methods: data analysis - techniques: image processing: large scale structure

## 1 INTRODUCTION

Weak gravitational lensing has been widely used as a direct probe of the large scale structure (see reviews by Bartelmann & Schneider 2001; Wittman 2002; Refregier 2003). By measuring the systematic distortions of background galaxy images, one can place constraints on the cosmological parameters (Bacon et al. 2000; Kaiser et al. 2000; van Waerbeke et al. 2000; Wittman et al. 2000; Maoli et al. 2001; Rhodes et al. 2001; van Waerbeke et al. 2001; Hoekstra et al. 2002; Refregier et al. 2002; Bacon et al. 2003; Brown et al. 2003; Hamana et al. 2003; Jarvis et al. 2003; Rhodes et al. 2004; Heymans et al. 2005; Massey et al. 2005; van Waerbeke et al. 2005; Dahle 2006; Hoekstra et al. 2006; Jarvis et al. 2006; Semboloni et al. 2006; Hettterscheidt et al. 2007; Schrabback et al. 2007). With accurate redshift information, the geometry and the structure growth rate of our Universe can be constrained as functions of redshift separately, providing a consistency test of the gravity theory (Hu 2002; Abazajian & Dodelson 2003; Jain & Taylor 2003; Acquaviva et al. 2004;

Bernstein & Jain 2004; Hu & Jain 2004; Kratochvil et al. 2004; Song & Knox 2004; Takada & Jain 2004; Takada & White 2004; Ishak 2005; Simpson & Bridle 2005; Song 2005; Zhang et al. 2005; Hannestad et al. 2006; Ishak et al. 2006; Zhan 2006; Knox et al. 2006; Schimd et al. 2007; Taylor et al. 2007).

A key issue in weak lensing is about how to measure the cosmic shear with galaxy shapes. This is difficult mainly because the signal-to-noise ratio of the measurement on one galaxy is typically only a few percent. It is therefore extremely important for any shear measurement method to carefully treat any possible systematic errors, including at least the following: the correction due to the image smearing by the point spread function (PSF, including the pixel response function); the photon noise; the pixelation effect due to the discrete nature of the CCD pixels. There have been a number of methods proposed to deal with the corrections due to the PSF (see Tyson et al. 1990; Bonnet & Mellier 1995; Kaiser et al. 1995; Luppino & Kaiser 1997; Hoekstra et al. 1998; Rhodes et al. 2000; Kaiser 2000; Bridle et al. 2001; Bernstein & Jarvis 2002; Refregier & Bacon 2003; Massey & Refregier 2005; Kuijken 2006; Nakajima & Bernstein 2007;

<sup>\*</sup> E-mail: jzhang@astro.berkeley.edu

Zhang 2008). However, the photon noise and the pixelation effect remain to be treated in a more systematic way.

In a recent work by Zhang (2008) (Z08 hereafter), a new and simple way of measuring the cosmic shear is found. Its main advantages includes: 1. it is mathematically simple; 2. it is free of assumptions on the morphologies of the galaxies and the PSF; 3. it enables us to probe the shear information from galaxy substructures, thereby improving the signal-to-noise ratio. These facts encourage us to extend the method further by including a treatment of the photon noise and the pixelation effect. Fortunately, we find that these two types of systematic errors can be treated in a simple and model-independent way based on the method of Z08. As will become clear later in this paper, the method we adopt to remove the noise contamination can also be considered in other shear measurement methods, and our treatment of the pixelation effect is generally useful for image processing of all purposes.

The paper is organized as follows: in §2, we briefly review the shear measurement method of Z08; in §3, we show how to treat the photon noise (in §3.1) and the pixelation effect (in §3.2) in weak lensing; in §4, we use computer-generated mock galaxy images to test the performance of our method; finally, we summarize in §5.

## 2 REVIEW OF THE SHEAR MEASUREMENT METHOD

Z08 proposes a way of measuring the cosmic shear with the spatial derivatives of the galaxy surface brightness field. To do so, let us define the surface brightness on the image plane as  $f_I(\vec{\theta}^I)$ , and that on the source plane as  $f_S(\vec{\theta}^S)$ , where  $\vec{\theta}^I$  and  $\vec{\theta}^S$  are the position angles on the image and source plane respectively. These quantities are related in a simple way as:

$$\begin{aligned} f_I(\vec{\theta}^I) &= f_S(\vec{\theta}^S) \\ \vec{\theta}^I &= \mathbf{A}\vec{\theta}^S \end{aligned} \quad (1)$$

where  $\mathbf{A}_{ij} = \delta_{ij} + \Phi_{ij}$ , and  $\Phi_{ij} = \partial\delta\theta_i^I/\partial\theta_j^S$  are the spatial derivatives of the lensing deflection angle. Matrix  $\mathbf{A}$  is often expressed in terms of the convergence  $\kappa = (\Phi_{xx} + \Phi_{yy})/2$  and the two shear components  $\gamma_1 = (\Phi_{xx} - \Phi_{yy})/2$  and  $\gamma_2 = \Phi_{xy}$ . Assuming the intrinsic galaxy image  $f_S(\vec{\theta}^S)$  is statistically isotropic, the shear components can be simply related to the derivatives of the surface brightness field as (Seljak & Zaldarriaga 1999):

$$\begin{aligned} \gamma_1 &= -\frac{1}{2} \frac{\langle (\partial_x f_I)^2 - (\partial_y f_I)^2 \rangle}{\langle (\partial_x f_I)^2 + (\partial_y f_I)^2 \rangle} \\ \gamma_2 &= -\frac{\langle \partial_x f_I \partial_y f_I \rangle}{\langle (\partial_x f_I)^2 + (\partial_y f_I)^2 \rangle} \end{aligned} \quad (2)$$

where the averages are taken over the galaxy.

Eq.[2] is useful only when the angular resolution of the observation is infinitely high. In practice, the observed galaxy surface brightness distribution  $f_O$  is always equal to the lensed galaxy image  $f_I$  convoluted with the PSF, *i.e.* :

$$f_O(\vec{\theta}) = \int d^2\vec{\theta}^I W(\vec{\theta} - \vec{\theta}^I) f_I(\vec{\theta}^I) \quad (3)$$

where  $W$  is the PSF. Z08 has shown how to modify eq.(2) when the PSF is an isotropic Gaussian function, which can be written as:

$$W(\vec{\theta}) = \frac{1}{2\pi\beta^2} \exp\left(-\frac{|\vec{\theta}|^2}{2\beta^2}\right) \quad (4)$$

where  $\beta$  is the scale radius of the Gaussian function. The new relation between the shear components and the derivatives of the surface brightness field is:

$$\begin{aligned} \gamma_1 &= -\frac{1}{2} \frac{\langle (\partial_x f_O)^2 - (\partial_y f_O)^2 \rangle}{\langle (\partial_x f_O)^2 + (\partial_y f_O)^2 \rangle + \Delta} \\ \gamma_2 &= -\frac{\langle \partial_x f_O \partial_y f_O \rangle}{\langle (\partial_x f_O)^2 + (\partial_y f_O)^2 \rangle + \Delta} \end{aligned} \quad (5)$$

where

$$\Delta = \frac{\beta^2}{2} \langle \vec{\nabla} f_O \cdot \vec{\nabla} (\nabla^2 f_O) \rangle \quad (6)$$

For a general PSF, one can transform it into the desired isotropic Gaussian form through a convolution in Fourier space. The scale radius  $\beta$  of the target PSF should be larger than that of the original PSF to avoid singularities in the convolution. Furthermore, as shown in Z08, the spatial derivatives required by eq.(5) can also be easily evaluated in Fourier space.

## 3 TREATING THE PHOTON NOISE AND THE PIXELATION EFFECT

In this section, we introduce the basic ideas for treating the photon noise and the pixelation effect in §3.1 and §3.2 respectively. Numerical examples are given in the next section.

### 3.1 Photon Noise

The presence of the photon noise makes the measurement of the cosmic shear more complicated in two ways: 1. the observed surface brightness  $f_O$  is from both the lensed source and the un-lensed foreground noise; 2. because of the aliasing power caused by the non-periodic boundaries of the *noisy* map, the measurement of the spatial derivatives of the surface brightness field cannot be accurately performed in Fourier space. As we show in the rest of this section, our master equation [eq.(5)] for estimating the cosmic shear can be easily adapted to solve both problems.

Before proceeding, it is useful to note that the first problem listed above is present in all of the existing shear measurement methods. This is because these methods are usually designed based on the analysis of the lensed source signals, instead of a mixture of the source and the noise (un-lensed). Simple treatments such as filtering out the noise outside of the source image do not completely fix this problem, because the noise inside the image can still bias the shear estimate.

In the method of Z08, to isolate the source signals in a noisy map, let us first write the total observed surface brightness  $f_O$  as the sum of the contributions from the source  $f^s$  and the noise  $f^n$ , *i.e.* ,  $f_O = f^s + f^n$ . Note that in this case, instead of  $f_O$ ,  $f^s$  should be used in eq.(5) to correctly measure the shear components. For this purpose, let us use the following relation:

$$\begin{aligned} \langle (\partial_x f^s)^2 \rangle &= \langle (\partial_x f_O)^2 \rangle - \langle (\partial_x f^n)^2 \rangle \\ &\quad - 2\langle \partial_x f^s \partial_x f^n \rangle \end{aligned} \quad (7)$$

$$\begin{aligned}
 \langle (\partial_y f^s)^2 \rangle &= \langle (\partial_y f_O)^2 \rangle - \langle (\partial_y f^n)^2 \rangle \\
 &\quad - 2\langle \partial_y f^s \partial_y f^n \rangle \\
 \langle \partial_x f^s \partial_y f^s \rangle &= \langle \partial_x f_O \partial_y f_O \rangle - \langle \partial_x f^n \partial_y f^n \rangle \\
 &\quad - \langle \partial_y f^s \partial_x f^n \rangle - \langle \partial_x f^s \partial_y f^n \rangle \\
 \langle \vec{\nabla} f^s \cdot \vec{\nabla} (\nabla^2 f^s) \rangle &= \langle \vec{\nabla} f_O \cdot \vec{\nabla} (\nabla^2 f_O) \rangle - \langle \vec{\nabla} f^n \cdot \vec{\nabla} (\nabla^2 f^n) \rangle \\
 &\quad - \langle \vec{\nabla} f^s \cdot \vec{\nabla} (\nabla^2 f^n) \rangle - \langle \vec{\nabla} f^n \cdot \vec{\nabla} (\nabla^2 f^s) \rangle
 \end{aligned}$$

For simplicity, in this paper, we only consider the photon noise that is from the foreground or the instruments. The surface brightness distribution of the noise is therefore uncorrelated with that of the background sources<sup>1</sup>. Under this assumption, the cross-correlations between the source and the noise terms (such as, *e.g.*,  $\langle \partial_x f^s \partial_x f^n \rangle$ ) should vanish. Eq.(7) therefore becomes:

$$\begin{aligned}
 \langle (\partial_x f^s)^2 \rangle &= \langle (\partial_x f_O)^2 \rangle - \langle (\partial_x f^n)^2 \rangle \\
 \langle (\partial_y f^s)^2 \rangle &= \langle (\partial_y f_O)^2 \rangle - \langle (\partial_y f^n)^2 \rangle \\
 \langle \partial_x f^s \partial_y f^s \rangle &= \langle \partial_x f_O \partial_y f_O \rangle - \langle \partial_x f^n \partial_y f^n \rangle \\
 \langle \vec{\nabla} f^s \cdot \vec{\nabla} (\nabla^2 f^s) \rangle &= \langle \vec{\nabla} f_O \cdot \vec{\nabla} (\nabla^2 f_O) \rangle - \langle \vec{\nabla} f^n \cdot \vec{\nabla} (\nabla^2 f^n) \rangle
 \end{aligned} \tag{8}$$

The relations in eq.(8) suggest an easy way of removing the contaminations from the photon noise: one can use a neighboring map of pure noise  $f^n$  to estimate  $\langle (\partial_x f^n)^2 \rangle$ ,  $\langle (\partial_y f^n)^2 \rangle$ ,  $\langle \partial_x f^n \partial_y f^n \rangle$ ,  $\langle \vec{\nabla} f^n \cdot \vec{\nabla} (\nabla^2 f^n) \rangle$ , and subtract them from their counterparts evaluated from the noisy source map  $f_O$  to get the source terms required by eq.(5). Note that since the noise photons are distributed differently in each map, the above procedure does not exactly remove the noise contribution for each source image. However, the method is statistically accurate as long as the statistical properties of the photon noise are stable over a reasonably large scale. In other words, the differences in the noise distributions of two maps add statistical errors to the measured cosmic shear through this procedure, but no systematic errors. Finally, the pure noise map should be a close neighbor of the source map so that they share the same point spread function.

To evaluate the derivatives of the surface brightness field of a noisy map in the Fourier space, we need to deal with the non-periodic boundaries appropriately to avoid aliasing powers. This can be done by gradually attenuating the noise towards the boundaries of the map. The attenuation can take an arbitrary form as long as the following criterions are satisfied: 1. the source region is not affected; 2. the edges of the map should be rendered sufficiently faint; 3. the attenuation amplitude should not have abrupt spatial variations; 4. to properly remove the noise contamination, the same attenuation should also be applied to the neighboring map of pure noise.

In §4, we show numerical examples to support the noise treatment discussed above.

### 3.2 The Pixelation Effect

Modern astronomical images are commonly recorded on CCD pixels, the discrete nature of which may affect the accuracy of the cosmic shear measurements. This is because

<sup>1</sup> More general cases (*e.g.*, photon noise coming from faint background sources) are more complicated, and will be dealt with in a future work.

all shear measurement methods developed so far are based on continuous surface brightness fields. In general, to avoid significant shear measurement errors, the pixel size should be at least a few times smaller than the scale radius (or FWHM) of the PSF. For instance, we find that the method of Z08 requires the scale radius of the PSF to be roughly 3 or 4 times larger than the pixel size. This requirement is often not satisfied in space-based observations. It is therefore useful to have a method which can reconstruct continuous images from under-sampled ones.

This is indeed a well-defined interpolation problem: how to reconstruct a continuous function if its value is only given at a set of discrete points. In the context of weak lensing, there is a quantitative way of testing the performance of the interpolation method, which is to check the accuracy of the shear recovery using the reconstructed images. The best method should yield the fastest convergence to an accurate image reconstruction (or shear recovery) as the pixel size becomes smaller.

We have tested several standard 2D interpolation methods, including Bilinear interpolation, Bicubic interpolation, and Bicubic Spline interpolation (see Press et al. 1992 for details). Although these conventional methods perform reasonably well, we find that they can all be significantly improved by interpolating the natural logarithms of the data instead of the data themselves. This is mainly due to two reasons: 1. the values of the data have a lower bound — zero; 2. at large distances, the PSF typically falls off exponentially. For convenience, in the rest of the paper, we call such extensions of the three classical interpolation methods their original names with the prefix “Log-”, and always abbreviate “Bicubic Spline” to “Spline”. The mathematical definitions of the six methods (*i.e.*, Bilinear, Bicubic, Spline, Log-Bilinear, Log-Bicubic, Log-Spline) are given in the appendix. In §4, we show that the Log-Bicubic and Log-Spline methods are most accurate among the six. As will be shown in our numerical examples, continuous images that are reconstructed by these two interpolation methods yield negligible systematic errors in shear recovery as long as the pixel size is about smaller than the PSF size (twice its scale radius). Note that the pixel size is *rarely* larger than the PSF size in practice, because the pixel response function is a part of the PSF.

## 4 NUMERICAL EXAMPLES

We present numerical examples to support the ideas introduced in the previous section. The general setup of our numerical simulations are given in §4.1. In §4.2 and §4.3, we test our treatments of the photon noise and the pixelation effect separately. Finally, the overall performance of our method is shown in §4.4.

### 4.1 General Setup

Each of our galaxy images is placed on a  $2^n \times 2^n$  grid, where  $n$  is an integer (typical chosen to be 8). Note that such a choice facilitates the Fast Fourier Transformation (FFT). Each grid point is treated as the location of the center of a CCD pixel, whose side length is equal to the grid size. All

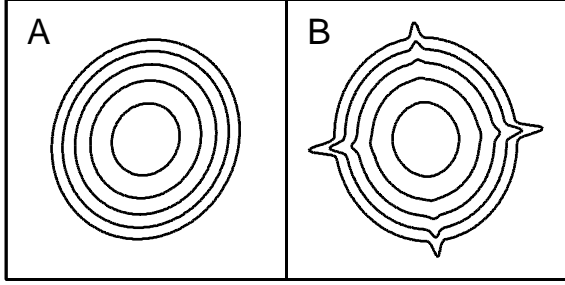


**Figure 1.** Two PSF forms used in this paper. The letter on the up-left corner of each plot is the label of the PSF defined in eq.(9) (rotated by certain angles). The contours mark 0.0025%, 0.025%, 0.25%, 2.5%, and 25% of the peak intensity.

sizes in our simulations are expressed in units of the grid size, *i.e.*, the pixel size.

The form of the PSF is chosen from the following two functions rotated by certain angles:

$$\begin{aligned}
 W_A(x, y) &\propto \exp \left[ -\frac{1}{2R_{PSF}^2} (x^2 + 0.8y^2) \right] \\
 W_B(x, y) &\propto \exp \left[ -\frac{1}{2R_{PSF}^2} (x^2 + 0.8y^2) \right] \\
 &+ 0.03 \exp \left[ -\left( \frac{x^2}{R_{PSF}^2} + 0.2 \right) \cdot \left( \frac{y^2}{R_{PSF}^2} + 0.2 \right) \right]
 \end{aligned} \quad (9)$$

where  $R_{PSF}$  is the scale radius of the PSF. A schematic view of the PSF functions is shown in fig.1. Note that the additional term in  $W_B$  mimics the diffraction spikes. As discussed in §2, before measuring the shear using eq.(5), the PSF is always transformed into the desired isotropic Gaussian form, whose scale radius  $\beta$  should be slightly larger than  $R_{PSF}$  defined here to avoid singularities in the transformation. Note that we have reserved the Greek letter  $\beta$  for the scale radius of the target PSF to distinguish it from  $R_{PSF}$ .

Both the galaxies and the noise are treated as collections of point sources. For example, the image of a galaxy in our simulation is typically made of a few hundred or thousand points. The advantage of doing so is that one can easily lense the galaxy by displacing its point sources and modifying their amplitudes. The intensities of the point sources are distributed to the neighboring grid points of their locations according to the PSF. For example, a point source of intensity  $A$  at location  $\vec{x}$  contributes an intensity of  $A \cdot W_{PSF}(\vec{y} - \vec{x})$  to the grid point at location  $\vec{y}$ . The total intensity on a grid point is the sum of contributions from all the point sources. Since everything is composed of point sources in our simulation, we will mostly call the surface brightness the flux density in the rest of the paper.

There are two types of mock galaxies we use in this paper: regular disk galaxies and irregular galaxies. Our regular galaxy contains a thin circular disk of an exponential profile and a co-axial de Vaucouleurs-type bulge (de Vaucouleurs et al. 1991). On average, its face-on surface brightness distribution is parameterized as:

$$f(r) \propto \exp(-r/r_{disk}) + f_{b/d} \exp \left[ -(r/r_{bulge})^{1/4} \right] \quad (10)$$

where  $r$  is the distance to the galaxy center,  $r_{bulge}$  and  $r_{disk}$  are the scale radii of the bulge and the disk respectively, and  $f_{b/d}$  determines the relative brightness of the bulge with respect to the disk. In the simulation, this profile is realized by properly and randomly placing a certain number (typically a few hundred) of point sources. These point sources are projected onto a randomly oriented image plane, lensed, and finally assigned to the CCD pixels according to the PSF to yield the galaxy image. Our irregular galaxies are generated by 2D random walks. The random walk starts from the center of the grid, and continues for a certain number of steps. Each step has a fixed size and a completely random orientation in the image plane. The joint of every two adjacent steps gives the pre-lensing position of a point source of the galaxy in the image plane. The resulting irregular galaxies usually contain abundant substructures.

For numerical manageability, we always cutoff the galaxy profile at a certain radius  $R_G$ , which is denoted as the scale radius of the galaxy. This is done by excluding the points that are outside of radius  $R_G$  in generating our regular galaxies. For the irregular galaxies, the random walker is sent back to the origin to continue from there when it reaches the radius  $R_G$ .

Without loss of generality, we set  $f_{b/d} = 1/3$ ,  $r_{disk}/r_{bulge} = 3$ , and  $r_{disk} = R_G$  for the regular galaxies.

## 4.2 Testing the Photon Noise Treatment

As our first example, we use 10000 mock regular galaxies to test the treatment of photon noise discussed in §3.1. Each galaxy is made of 600 point sources. The galaxy size  $R_G$  is fixed at 30. The angle between the line-of-sight direction and the normal vector of the disk plane is randomly chosen from  $[0, \pi/6]$ . The PSF we use is  $W_A$  of eq.(9) with  $R_{PSF} = 4$  (no pixelation effect). The scale radius  $\beta$  of the target isotropic Gaussian PSF is 6. The noise is made of Poisson distributed point sources, the mean number density of which is roughly one per  $4 \times 4$  area. Each point source of the noise is given the same intensity, the value of which can be freely adjusted to determine the ratio of the mean flux density of the noise to that of the galaxy (within its scale radius). Fig.2 shows sample images of four different noise-to-galaxy flux density ratios: 0.02, 0.1, 0.5, 1.5. To avoid aliasing powers in Fourier transformation, the noise near the boundaries of the map is filtered out by a window function defined as follows:

$$W_{filter}(r) = \begin{cases} 1 & \text{if } r \leq R_{core}; \\ \exp \left[ -\frac{1}{2} \left( \frac{r - R_{core}}{R_{width}} \right)^2 \right] & \text{if } r > R_{core}. \end{cases}$$

where  $r$  is the distance to the map/galaxy center,  $R_{core}$  is the radius encircling the unaffected region, and  $R_{width}$  determines the width of the transition area. Note that the flat core of the filter should be sufficiently large to avoid affecting the galaxy images. In our simulations, we always choose  $R_{core} = R_G + 4\beta$ , and  $R_{width} = \beta$ . Finally, to correct for the noise, for each galaxy map, we generate a map of pure noise to measure the noise properties required by eq.(8). The same filter is also applied to the pure noise map before the Fourier transformation.

In fig.3, we plot the recovered shear values for different noise-to-galaxy flux density ratios  $I_N/I_G$ . The input cosmic

shear  $(\gamma_1, \gamma_2)$  is  $(0.023, -0.037)$ , displayed as dotted lines. The red data points with  $1\sigma$  error bars are our main results achieved through the complete treatment of noise. For a comparison, the blue ones show the shear values measured directly from the noisy galaxy maps using eq.(5) without correcting for the noise (but the filter given by eq.(11) is still applied to avoid the aliasing power in Fourier transformation). The figure clearly demonstrates that our noise treatment works remarkably well even when the mean flux density of the noise is comparable with that of the galaxy, though we caution that the size of the error bar grows with increasing noise intensity. On the other hand, the blue data points indicates that without a proper treatment of the noise, the measured shear values quickly drops to zero as the noise flux becomes dominant, deviating significantly from the input shear values.

Finally, it is worth noting that both here and in the simulations reported in the rest of the paper, the number density of the noise points is always chosen to be roughly one point per PSF area ( $\sim R_{PSF}^2$ ) or slightly more. This is due to two reasons: 1. for a fixed mean noise flux density, a higher number density of the Poisson distributed noise points indeed leads to lower spatial fluctuations of the noise surface brightness field, therefore a less contamination to the shear signal, or a less challenging condition; 2. On the other hand, if the number density is much smaller than one point per PSF area, the image turns into a collection of discrete point-like sources, causing both the nominator and the denominator of eq.(5) to become small differences of large numbers, which are well known sources for numerical errors. The second point simply means it is hard to measure the shapes of sources that are much smaller than the size of the PSF. In practice, we can avoid the second situation by increasing the observation/integration time.

### 4.3 Testing the Treatment of the Pixelation Effect

When the scale radius of the PSF is less than 3 or 4 times the pixel size, the galaxy/noise images start to look pixelated, and the shear recovery accuracy may be strongly affected by the discrete nature of the CCD pixels. To reconstruct continuous images, we use 2D interpolation methods to insert finer grid points. The finer grid size is chosen to be  $2^m$  ( $m$  is an integer) times smaller than the original grid size, and at least less than a quarter of the PSF scale radius  $R_{PSF}$ . It is worth noting that interpolation of the pixelated image, if necessary, is always the first step in our shear measurement procedure.

An example of a pixelated image is shown in the up-left corner of fig.4, for which the scale radius of the PSF is 0.5. The high resolution images reconstructed by the three interpolation methods and their logarithmic extensions discussed in §3.2 are show in the lower half of fig.4. The true high resolution image is on the up-right corner of the figure. By simply comparing the morphologies of the interpolated images by eye, one may already tend to conclude that the performances of the three conventional methods are improved if we interpolate the log of the data instead of the data itself. For instance, negative intensities (denoted as blue regions in the figure) are commonly found in the interpolated maps by the Bicubic and Spline methods, but absent in those by the Log-Bicubic or Log-Spline methods;

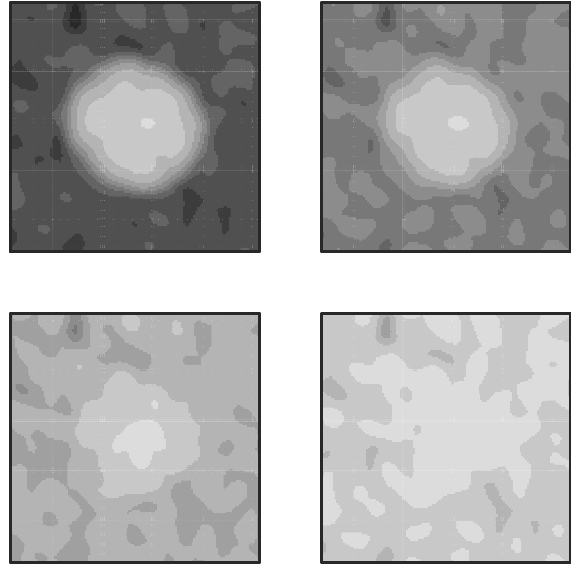


**Figure 2.** Sample images of four different noise-to-galaxy flux density ratios. The up-left, up-right, lower-left, lower-right plots are for flux density ratios of 0.02, 0.1, 0.5, 1.5 respectively.

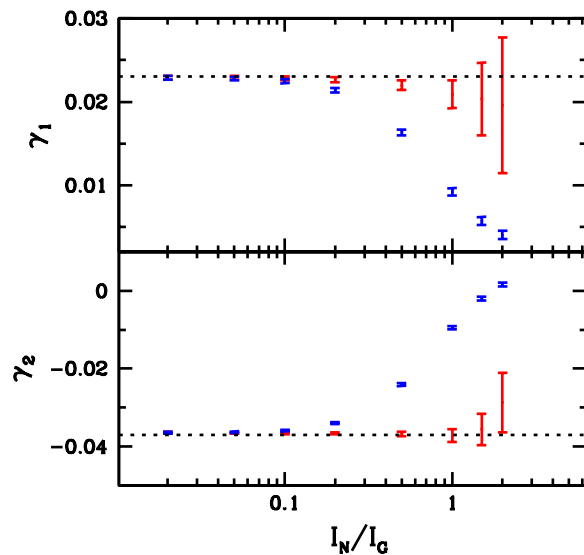


**Figure 3.** The shear values with  $1\sigma$  error bars measured from images of different noise-to-galaxy flux density ratios  $I_N/I_G$ . The measurement uses 10000 mock regular galaxies. The dotted lines indicate the input shear values. The red data points are our main results achieved through the complete treatment of noise introduced in §3.1. The blue ones show the shear values measured directly from the noisy galaxy maps using eq.(5) without removing the noise contaminations.

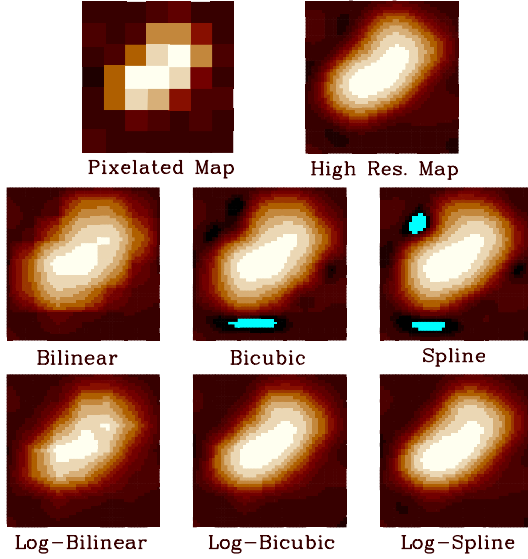


**Figure 4.** The example of a pixelated image (upper-left), its high resolution counterpart (upper-right), and its interpolated images by the Bilinear, Bicubic, Spline, Log-Bilinear, Log-Bicubic, and Log-Spline methods (middle and lower panels). The blue regions have negative intensities.

the filamentary features produced by the Bilinear method become somewhat less prominent in the map processed by the Log-Bilinear method.

To test the interpolation methods more quantitatively, we may compare the shear values measured from the interpolated maps using eq.(5) (in the absence of noise). Clearly, all the interpolation methods should yield the same and correct shear estimates for a given galaxy and PSF if the PSF scale radius is much larger than the pixel size, *i.e.*, in the absence of the pixelation effect. For small PSF sizes, as we have seen, the continuous images interpolated by different methods look unlike each other, resulting in possibly very different shear values. Moreover, since the source is sparsely sampled in this case, the original (pixelated) image, the interpolated image, and the measured shear values all depend on the relative positions of the pixels with respect to the source. In fig.5, we show the distributions (as histograms) of the shear values estimated from a *single* galaxy that is placed at different/random locations on the grid. For simplicity and clarity, we do not include any photon noise here. The ratio of the galaxy size  $R_G$  to the PSF scale radius  $R_{PSF}$  is fixed at 5. The ratio of the pixel size to  $R_{PSF}$  is chosen to be 2, 1.5, 1, 0.5, the results of which are represented by the purple, blue, red, and black histograms respectively. The figure shows that as the pixel size decreases relative to the PSF size, the shear distributions converge more rapidly to a delta function at the correct position in methods with the prefix “Log-”, manifesting again the value of the logarithmic extensions of the three classic interpolation methods.

Finally, let us find out which interpolation method is best suited to weak lensing. For this purpose, we test the accuracy of shear recovery with a large number of interpolated galaxy images. To make it a more convincing test, we use our morphologically rich irregular galaxies, each of

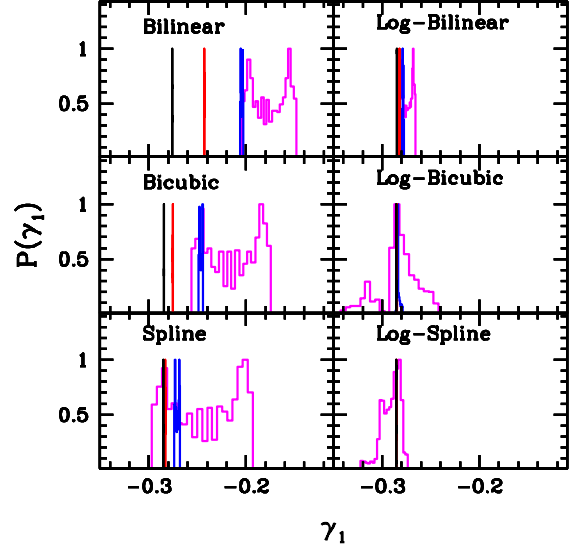


**Figure 5.** The distribution of the shear values measured from the interpolated images of a *single* galaxy placed at random positions on the grid. The purple, blue, red, and black histograms correspond to the pixel-size-to-PSF-radius ratio of 2, 1.5, 1, 0.5 respectively. Each panel shows the results from a single interpolation method, whose name is indicated in the upper-left corner of the plot. All the histograms are normalized so that their peak values are one.

which is generated by 1000 random steps. We consider three choices for the random walk step size and the galaxy scale radius  $R_G$ :  $(0.5R_{PSF}, 6.67R_{PSF})$ ,  $(0.25R_{PSF}, 3.33R_{PSF})$ , and  $(0.125R_{PSF}, 1.67R_{PSF})$ , referring to large, medium, and small galaxies respectively. The PSF we use is  $W_B$ .  $\beta$  of the target isotropic Gaussian PSF is set to be  $4/3$  of  $R_{PSF}$ . The cosmic shear  $(\gamma_1, \gamma_2)$  is chosen to be  $(-0.031, 0.018)$ . No photon noise is included. Our results are summarized in fig.6, in which we plot the measured shear values against the ratio of the pixel size to  $R_{PSF}$ . In the upper, middle, and lower panels of the figure, we report the results from averaging over 10000 large, medium, and small size galaxies respectively. The dotted lines refer to the input shear values. The cyan, blue, magenta, green, red, and black data points with  $1\sigma$  error bars are from the Bilinear, Bicubic, Spline, Log-Bilinear, Log-Bicubic, and Log-Spline methods respectively. According to the figure, we can draw several conclusions:

1. As a sanity check, we confirm that all the interpolation methods work well when the PSF size is much larger than the pixel size;

2. Log-Bicubic and Log-Spline are the two most successful methods. Both of them can correctly recover the input shear as long as  $R_{PSF}$  is about larger than a half of the pixel size, regardless of the galaxy size. Note that one should not expect any interpolation method to work well when  $R_{PSF} \ll 0.5$  unless the source images are sufficiently smooth over the scale of the pixel size.

3. The pixelation effect is less important for larger galaxies. For instance, by comparing the results in the three panels of fig.6, we see that the quality of shear recovery becomes increasingly poor for galaxies of smaller sizes for

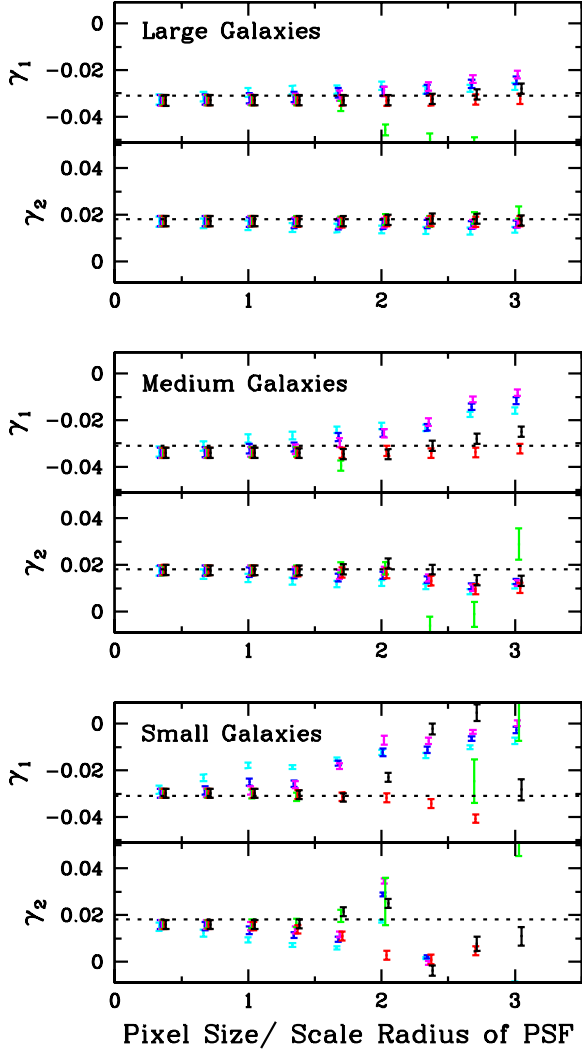


**Figure 6.** The measured shear values plotted against the ratio of the pixel size to the PSF scale radius  $R_{PSF}$ . The upper, middle, and lower windows show the results from averaging over 10000 relatively large, medium, and small size galaxies respectively. The definition of the galaxy size in this example can be found in §4.3. The cyan, blue, magenta, green, red, and black data points with  $1\sigma$  error bars are the results from the Bilinear, Bicubic, Spline, Log-Bilinear, Log-Bicubic, and Log-Spline interpolation methods respectively. The input shear values are shown as dotted lines.

a given  $R_{PSF}$ . This is not surprising because the structures/shapes of large galaxies are better resolved than those of smaller ones. Meanwhile, it is encouraging to note that the Log-Bicubic and Log-Spline methods perform fairly well for  $R_{PSF} \gtrsim 0.5$  even when the galaxy size is comparable to the PSF size.

#### 4.4 Testing the Overall Performance

The purpose of this section is to test our shear measurement method under general conditions, *i.e.*, in the presence of both photon noise and the pixelation effect. Fig.7 shows the pipeline of the numerical procedures we take in general

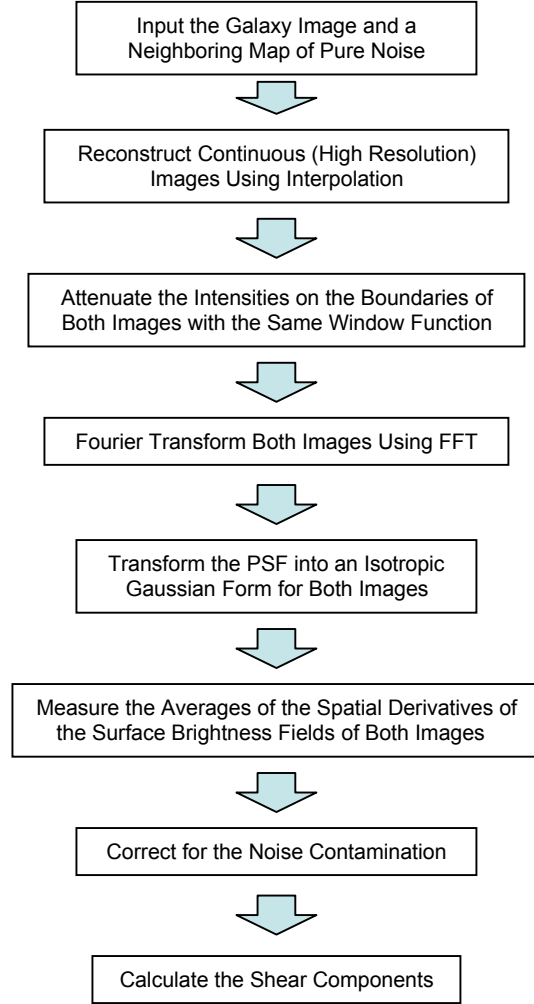


**Figure 7.** The pipeline of our shear measurement procedures in the presence of both the photon noise and the pixelation effect.

cases. A detailed explanation of each item in the graph has been given in §3.

In Table 1, we show the shear recovery results of ten examples, each of which uses 10000 mock regular/irregular galaxies. The columns from the left to the right specify the input shear values, the galaxy type, the PSF type, the ratio of the galaxy size to the PSF size ( $R_G/R_{PSF}$ ), the ratio of the mean flux density of the noise to that of the galaxy ( $I_N/I_G$ ), the PSF scale radius ( $R_{PSF}$ ), the interpolation method, and the measured shear values with  $1\sigma$  errors respectively. In each example, the same set of galaxies are used under two conditions: 1. the ideal condition, in which the noise surface brightness  $I_N$  is set to zero, and  $R_{PSF} = 4$ , so that no interpolations or noise treatments are required; 2. the challenging condition, in which the noise flux density is comparable with those of the galaxies, and  $R_{PSF} \sim 0.5$ . In the table, we show the shear values measured under both conditions. For the challenging case in each example, the results are reported in two rows, which are achieved using the Log-Bicubic and the Log-Spline interpolation methods respectively. In all the examples, the scale radius of the target

isotropic Gaussian PSF is  $1.5R_{PSF}$ . To avoid aliasing powers in Fourier transformation, we use eq.(11) to filter the noise near the boundaries of the map.

The data in the table show that the input shear values can be accurately recovered under both the ideal and the challenging conditions. The Log-Bicubic and the Log-Spline methods work almost equally well. The number of those measured shears that are more than  $1\sigma$  away from the input ones (written in red color in the table for clarity) is about 30% of the total, very close to its statistical expectation value ( $\sim 32\%$ ).

## 5 SUMMARY

We have discussed how to correct for the systematic errors due to the photon noise and the pixelation effect in cosmic shear measurements. Our treatment of photon noise allows us to reliably remove the noise contamination to the cosmic shear even when the noise flux density is comparable with that of the sources. In principle, our method works regardless of the brightness of the noise, though when the noise is much brighter than the sources, one needs to worry about image selections, which will be discussed in a separate paper. To deal with pixelated images, our approach is to reconstruct continuous images by interpolating the natural logarithms of the pixel readouts with either the Bicubic or Bicubic Spline method. This technique is accurate for the purpose of shear recovery as long as the scale radius of the PSF is larger than about a half of the pixel size, a condition which is almost always satisfied in practice.

Despite the fact that our study has been based on the shear measurement method of Z08, a part of our methodology is generally useful for other shear measurement methods, or even other astronomical measurements as well. The most obvious thing to note is that the Log-Bicubic and Log-Spline interpolation methods are accurate image reconstruction approaches not only for weak lensing, but also for all kinds of other purposes. The way we remove the noise contamination from the shear signal can in principle also be considered in other shear measurements, in particular those that are based on measuring the multipole moments of the source images (*e.g.*, Kaiser et al. 1995 and its various extensions).

The systematic errors we have neglected so far include the high order corrections (*e.g.*,  $\gamma^2$ ,  $\kappa^2$ ,  $\gamma\kappa$ ) to our master equation [eq.(5)], the spatial variations of the cosmic shear, etc.. These factors likely affect the measured shear values at a few percent levels, which is important in the era of precision cosmology. This subject will be studied in a companion paper.

This paper is a natural continuation of Z08 on the methodology of cosmic shear measurement. In another paper, we will further test this method with the data from the Shear TESting Program (Heymans et al. 2006; Massey et al. 2007), and present results measured with real astronomical data.

## ACKNOWLEDGEMENTS

JZ is supported by NASA, and by the TAC Fellowship of UC Berkeley.

## REFERENCES

- Abazajian K. & Dodelson S., 2003, PRL, 91, 041301  
 Acquaviva V., Baccigalupi C. & Perrotta F., 2004, PRD, 70, 023515  
 Bacon D., Massey R., Refregier A., Ellis R., 2003, MNRAS, 344, 673  
 Bacon D., Refregier A. & Ellis R., 2000, MNRAS, 318, 625  
 Bartelmann M. & Schneider P., 2001, Physics Reports, 340, 291  
 Bernstein G. & Jain B., 2004, ApJ, 600, 17  
 Bernstein G. & Jarvis M., 2002, AJ, 123, 583  
 Bonnet H. & Mellier Y., 1995, A&A, 303, 331  
 Bridle S., Gull S., Bardeau S., Kneib J., 2001, in Scientific N. W., ed., Proceedings of the Yale Cosmology Workshop  
 Brown M., Taylor A., Bacon D., Gray M., Dye S., Meisenheimer K., Wolf C., 2003, MNRAS, 341, 100  
 Dahle H., 2006, ApJ, 653, 954  
 Hamana T. et al., 2003, ApJ, 597, 98  
 Hannestad S., Tu H. & Wong Y., 2006, JCAP, 0606, 025  
 Hettterscheidt M., Simon P., Schirmer M., Hildebrandt H., Schrabback T., Erben T., Schneider P., 2007, A&A, 468, 859  
 Heymans C. et al., 2005, MNRAS, 361, 160  
 Heymans C. et al., 2006, MNRAS, 368, 1323  
 Hoekstra H., Franx M., Kuijken K., Squires G., 1998, ApJ, 504, 636  
 Hoekstra H., 2006, ApJ, 647, 116H  
 Hoekstra H., Yee H. & Gladders M., 2002, ApJ, 577, 595  
 Hu W., 2002, PRD, 66, 083515  
 Hu W. & Jain B., 2004, PRD, 70, 043009  
 Ishak M., 2005, MNRAS, 363, 469  
 Ishak M., Upadhye A. & Spergel D., 2006, PRD, 74, 043513  
 Jain B. & Taylor A., 2003, PRL, 91, 141302  
 Jarvis M., Bernstein G., Jain B., Fischer P., Smith D., Tyson J., Wittman D., 2003, ApJ, 125, 1014  
 Jarvis M., Jain B., Bernstein G., Dolney D., 2006, ApJ, 644, 71  
 Kaiser N., 2000, ApJ, 537, 555  
 Kaiser N., Squires G. & Broadhurst T., 1995, ApJ, 449, 460  
 Kaiser N., Wilson G. & Luppino G., astro-ph/0003338  
 Knox L., Song Y. & Tyson J., 2006, PRD, 74, 023512  
 Kratochvil J., Linde A., Linder E., Shmakova M., 2004, JCAP, 0407, 001  
 Kuijken K., 2006, A&A, 456, 827K  
 Luppino G. & Kaiser N., 1997, ApJ, 475, 20  
 Maoli R., van Waerbeke L., Mellier Y., Schneider P., Jain B., Bernardeau F., Erben T., 2001, A&A, 368, 766  
 Massey R., Bacon D., Refregier A., Ellis R., 2005, MNRAS, 359, 1277  
 Massey R. et al., 2007, MNRAS, 376, 13  
 Massey R. & Refregier A., 2005, MNRAS, 363, 197  
 Nakajima R. & Bernstein G., 2007, AJ, 133, 1763  
 Press W., Flannery B., Teukolsky S., Vetterling W., 1992, *Numerical Recipes*, Cambridge Univ. Press, 2nd ed.  
 Refregier A., 2003, ARA&A, 41, 645  
 Refregier A. & Bacon D., 2003, MNRAS, 338, 48  
 Refregier A., Rhodes J. & Groth E., 2002, ApJL, 572, L131  
 Rhodes J., Refregier A., Collins N., Gardner J., Groth E., Hill R., 2004, ApJ, 605, 29  
 Rhodes J., Refregier A. & Groth E., 2000, ApJ, 536, 79



Input ( $\gamma_1, \gamma_2$ )	Galaxy Type	PSF Type	$\frac{R_G}{R_{PSF}}$	$\frac{I_N}{I_G}$	$R_{PSF}$	Interpolation Method	Measured ( $\gamma_1, \gamma_2$ ) with $1\sigma$ error
(0.04, 0.01)	regular	$W_B$	7.5	0	4	(Not Required)	$(0.0449 \pm 0.0032, 0.0128 \pm 0.0032)$
				0.1	0.5	Log-Bicubic	$(0.0448 \pm 0.0030, 0.0126 \pm 0.0031)$
				0.1	0.5	Log-Spline	$(0.0463 \pm 0.0033, 0.0131 \pm 0.0033)$
(0.03, 0.05)	regular	$W_B$	2.5	0	4	(Not Required)	$(0.0279 \pm 0.0017, 0.0478 \pm 0.0017)$
				0.3	0.67	Log-Bicubic	$(0.0268 \pm 0.0021, 0.0470 \pm 0.0021)$
				0.3	0.67	Log-Spline	$(0.0278 \pm 0.0022, 0.0490 \pm 0.0022)$
(-0.02, 0.02)	irregular	$W_B$	10	0	4	(Not Required)	$(-0.0192 \pm 0.0021, 0.0200 \pm 0.0021)$
				0.4	0.5	Log-Bicubic	$(-0.0172 \pm 0.0021, 0.0192 \pm 0.0021)$
				0.4	0.5	Log-Spline	$(-0.0185 \pm 0.0021, 0.0200 \pm 0.0021)$
(-0.01, 0.05)	regular	$W_B$	10	0	4	(Not Required)	$(-0.0111 \pm 0.0013, 0.0506 \pm 0.0013)$
				0.6	0.57	Log-Bicubic	$(-0.0110 \pm 0.0013, 0.0501 \pm 0.0013)$
				0.6	0.57	Log-Spline	$(-0.0111 \pm 0.0014, 0.0504 \pm 0.0014)$
(-0.03, -0.06)	irregular	$W_A$	3.75	0	4	(Not Required)	$(-0.0315 \pm 0.0025, -0.0584 \pm 0.0025)$
				0.3	0.67	Log-Bicubic	$(-0.0292 \pm 0.0026, -0.0572 \pm 0.0026)$
				0.3	0.67	Log-Spline	$(-0.0331 \pm 0.0027, -0.0602 \pm 0.0027)$
(0.01, -0.02)	irregular	$W_A$	5	0	4	(Not Required)	$(0.0105 \pm 0.0022, -0.0228 \pm 0.0022)$
				0.4	0.67	Log-Bicubic	$(0.0118 \pm 0.0022, -0.0216 \pm 0.0022)$
				0.4	0.67	Log-Spline	$(0.0113 \pm 0.0023, -0.0223 \pm 0.0023)$
(0, 0)	regular	$W_A$	2.5	0	4	(Not Required)	$(0.0001 \pm 0.0012, -0.0006 \pm 0.0012)$
				0.5	0.5	Log-Bicubic	$(0.0033 \pm 0.0030, -0.0005 \pm 0.0032)$
				0.5	0.5	Log-Spline	$(0.0035 \pm 0.0033, 0.0001 \pm 0.0035)$
(0, -0.035)	irregular	$W_A$	7.5	0	4	(Not Required)	$(0.0012 \pm 0.0025, -0.0368 \pm 0.0025)$
				0.6	0.67	Log-Bicubic	$(0.0014 \pm 0.0024, -0.0358 \pm 0.0024)$
				0.6	0.67	Log-Spline	$(0.0008 \pm 0.0025, -0.0367 \pm 0.0025)$
(-0.05, -0.02)	irregular	$W_B$	15	0	4	(Not Required)	$(-0.0521 \pm 0.0019, -0.0212 \pm 0.0019)$
				0.2	0.67	Log-Bicubic	$(-0.0510 \pm 0.0019, -0.0209 \pm 0.0019)$
				0.2	0.67	Log-Spline	$(-0.0523 \pm 0.0019, -0.0212 \pm 0.0019)$
(0.06, -0.05)	irregular	$W_A$	15	0	4	(Not Required)	$(0.0589 \pm 0.0012, -0.0514 \pm 0.0012)$
				0.8	0.67	Log-Bicubic	$(0.0571 \pm 0.0013, -0.0502 \pm 0.0012)$
				0.8	0.67	Log-Spline	$(0.0582 \pm 0.0013, -0.0511 \pm 0.0013)$

**Table 1.** Ten examples showing how well the input shear values are recovered under both ideal (no noise, large PSF size) and challenging (large noise, small PSF size) conditions. Each example uses 10000 mock galaxies. For the challenging condition in each example, we show two sets of shear values measured using the Log-Bicubic and the Log-Spline interpolation methods respectively. The results in red color are more than  $1\sigma$  away from their input values.

Rhodes J., Refregier A. & Groth E., 2001, ApJL, 552, L85  
 Schimd C. et al., 2007, A&A, 463, 405  
 Schrabback T. et al., 2007, A&A, 468, 823  
 Seljak U. & Zaldarriaga M., 1999, PRL, 82, 2636  
 Semboloni E. et al., 2006, A&A, 452, 51  
 Simpson F. & Bridle S., 2005, PRD, 71, 083501  
 Song Y. & Knox L., 2004, PRD, 70, 063510  
 Song Y., 2005, PRD, 71, 024026  
 Takada M. & Jain B., 2004, MNRAS, 348, 897  
 Takada M. & White M., 2004, ApJ, 601, L1  
 Taylor A., Kitching T., Bacon D., Heavens A., 2007, MNRAS, 374, 1377  
 Tyson J., Wenk R. & Valdes F., 1990, ApJL, 349, L1  
 de Vaucouleurs G., de Vaucouleurs A., Corwin H., Buta R., Paturel G., Fouqué P., 1991, *Third Reference Catalogue of Bright Galaxies*, Springer, New York  
 van Waerbeke L. et al., 2000, A&A, 358, 30  
 van Waerbeke L., Mellier Y. & Hoekstra H., 2005, A&A, 429, 75  
 van Waerbeke L. et al., 2001, A&A, 374, 757

Wittman D., 2002, *Dark Matter and Gravitational Lensing, LNP Top. Vol.*, eds. Courbin F., Minniti D., Springer-Verlag., astro-ph/0208063  
 Wittman D., Tyson J., Kirkman D., Dell'Antonio I., Bernstein G., 2000, Nature, 405, 143  
 Zhan H., 2006, JCAP, 0608, 008  
 Zhang J., Hui L. & Stebbins A., 2005, ApJ, 635, 806  
 Zhang J., 2008, MNRAS, 383, 113

## APPENDIX – DEFINITIONS OF THE INTERPOLATION METHODS

In this appendix, we give the mathematical definitions of the three classic 2D interpolation methods: Bilinear, Bicubic, Spline. For their logarithmic extensions (*i.e.*, Log-Bilinear, Log-Bicubic, Log-Spline), we only have one minor point to address at the end of this section.

The Bilinear method is the simplest of the three. Let us write the coordinates of the grid points as  $(x_i, y_j)$  ( $i, j =$

1, 2, 3...), and the signals as  $A(x_i, y_j)$ . Suppose the point of our interest is  $(x, y)$ , which satisfies  $x_i \leq x \leq x_{i+1}$  and  $y_j \leq y \leq y_{j+1}$ , the Bilinear method defines  $A(x, y)$  in the following way:

$$A(x, y) = tuA(x_{i+1}, y_{j+1}) + (1-t)uA(x_i, y_{j+1}) \\ + t(1-u)A(x_{i+1}, y_j) + (1-t)(1-u)A(x_i, y_j) \quad (11)$$

where

$$t = (x - x_i)/(x_{i+1} - x_i) \quad (12) \\ u = (y - y_j)/(y_{j+1} - y_j).$$

The Bicubic method includes higher order terms of  $t$  and  $u$  to achieve smoothness of the interpolated function. It requires the user to specify not only the signal  $A(x_i, y_j)$ , but also the spatial derivatives  $\partial A/\partial x$ ,  $\partial A/\partial y$ , and  $\partial^2 A/\partial x \partial y$  at every grid point  $(x_i, y_j)$ . Since the spatial derivatives of the signal are usually not known a priori, we estimate them using the finite-difference method:

$$\frac{\partial A}{\partial x}(x_i, y_j) = \frac{A(x_{i+1}, y_j) - A(x_{i-1}, y_j)}{x_{i+1} - x_{i-1}} \quad (13) \\ \frac{\partial A}{\partial y}(x_i, y_j) = \frac{A(x_i, y_{j+1}) - A(x_i, y_{j-1})}{y_{j+1} - y_{j-1}} \\ \frac{\partial^2 A}{\partial x \partial y}(x_i, y_j) = [A(x_{i+1}, y_{j+1}) + A(x_{i-1}, y_{j-1}) \\ - A(x_{i+1}, y_{j-1}) - A(x_{i-1}, y_{j+1})] \\ / [(x_{i+1} - x_{i-1})(y_{j+1} - y_{j-1})]$$

The interpolated function inside each grid square is written in the following polynomial form:

$$A(x, y) = \sum_{m=1}^4 \sum_{n=1}^4 c_{mn} t^{m-1} u^{n-1} \quad (14)$$

The values of the sixteen parameters  $c_{mn}$  are constrained using eq.(14) and the following three equations at the four corners of the grid square:

$$\frac{\partial A}{\partial x}(x, y) = \sum_{m=2}^4 \sum_{n=1}^4 (m-1)c_{mn} t^{m-2} u^{n-1} \frac{dt}{dx} \quad (15) \\ \frac{\partial A}{\partial y}(x, y) = \sum_{m=1}^4 \sum_{n=2}^4 (n-1)c_{mn} t^{m-1} u^{n-2} \frac{du}{dy} \\ \frac{\partial^2 A}{\partial x \partial y}(x, y) = \sum_{m=2}^4 \sum_{n=2}^4 (m-1)(n-1)c_{mn} t^{m-2} u^{n-2} \frac{dt}{dx} \frac{du}{dy}$$

where  $t$  and  $u$  have been defined in eq.(12).

The 2D Spline method simply refers to using the 1D Spline interpolation along each dimension. The 1D (cubic) Spline interpolation method works as follows:

Given the values of a function  $f(x)$  at a set of points  $x_i$  ( $i = 1 \dots N$ ), the form of the function in the interval between  $x_j$  and  $x_{j+1}$  is written as:

$$f(x) = Hf(x_j) + Kf(x_{j+1}) + Uf''(x_j) + Vf''(x_{j+1}) \quad (16)$$

where

$$H = \frac{x_{j+1} - x}{x_{j+1} - x_j} \quad (17) \\ K = 1 - H$$

$$U = \frac{1}{6}(H^3 - H)(x_{j+1} - x_j)^2 \\ V = \frac{1}{6}(K^3 - K)(x_{j+1} - x_j)^2$$

and  $f''(x_j)$  is the second derivative of the function  $f$  at  $x_j$ . As a consistency check, one can easily show that  $d^2 f/dx^2 = Hf''(x_j) + Kf''(x_{j+1})$ . The value of the second derivatives are specified by requiring the first derivatives evaluated from the two sides of the grid point to be equal. Note that this requirement only provides  $N-2$  equations, while there are  $N$  second derivatives in total. The rest of the constraint comes from the boundary conditions on  $f''(1)$  and  $f''(N)$ . In this paper, we simply set  $f''(1) = f''(N) = 0$ , which yields the so-called *natural cubic spline*.

Finally, we note that the ‘‘Log’’ based interpolation methods are all well defined except when the readouts of some pixels are zero. This is a very rare case in practice due to the presence of noise. However, this situation can in principle exist in simulations. To cure this problem, one can either change the zeros into tiny positive numbers, or simply avoid interpolating the regions with zeros. The second option says that if a grid square (regarding the Log-Bilinear and Log-Bicubic methods) or a unitary segment (regarding the Log-Spline method) contains any zero readouts in their four corners or two ends, the finer grid points within them are all set to have zero values. The rest of the grid squares/segments are interpolated independently as usual. Note that in the Log-Spline method, this means the Spline interpolations are carried out only in those nonzero segments that are isolated by the zeros. These two choices usually work similarly well. However, when there are extended regions of zero readouts, we find that the second option is better, because it avoids introducing artificial high order fluctuations in the zero regions by methods like Log-Bicubic or Log-Spline.